

# Vibration-assisted annular fluid displacement for rig-less well abandonment operations

Hans Joakim Skadsem<sup>a,b,\*</sup>, Knut Erik Teigen Giljarhus<sup>a</sup>, Fiona Øijordsbakken Fredheim<sup>a,b</sup>, Egbert van Riet<sup>c</sup>, Wout J.G. Keultjes<sup>c</sup>

<sup>a</sup> University of Stavanger, P.O. Box 8600, 4036 Stavanger, Norway

<sup>b</sup> NORCE, Norwegian Research Centre AS, P.O. Box 8046, 4068 Stavanger, Norway

<sup>c</sup> Wells Technology, Shell Global Solutions International B. V., Grasweg 31, 1031HW Amsterdam, The Netherlands

## ARTICLE INFO

### Keywords:

Well decommissioning  
Vibration  
Annular displacement  
Completions  
Tubing

## ABSTRACT

Through-tubing abandonment is the operation where the production tubing is cut or punched and cemented inside the production casing. This can establish a full cross-sectional barrier or isolation in wells where the cement behind the production casing provides zonal isolation. Furthermore, isolation in the form of a through-tubing abandonment plug can be placed from a light-well intervention vessel, which reduces the risk and carbon footprint compared to conventional abandonment designs that rely on a full mobile offshore drilling unit. A potential challenge involved in placing the through-tubing abandonment plug is the risk of incomplete fluid displacement from the annulus behind the tubing: The tubing eccentricity may be considerable where the barrier should be placed, and the original packer fluid may be contaminated resulting in unfavorable displacement conditions. Furthermore, the tubing cannot be reciprocated or rotated to compensate for these conditions.

Agitator tools that generate lateral and axial vibrations in the tubing for mitigating potentially adverse displacement conditions have recently become available to the industry. We study potential effects of such tools by performing annular displacement experiments using a novel test rig that enables lateral movement of the inner tubing. The original fluid to be displaced was viscified with a polymer additive to generate apparent yield stress behavior and to thereby develop challenging displacement conditions, particularly in the eccentric annulus. Experimental results and supporting numerical simulations show that lateral motion of the tubing is effective in displacing the yield stress fluid from the narrow side of the eccentric annulus, and to oppose the tendency toward stratification in both concentric and eccentric annuli. The experiments further show that vibration is effective in improving the displacements at inclinations ranging from vertical to 80° from the vertical, and that high frequency vibrations are more effective than lower frequency vibrations at the same amplitude. Results from a mechanical vibration analysis suggests the vibration amplitudes increase with increasing flow rates, and that potentially beneficial vibrations can propagate over axial lengths that are comparable or longer than minimum barrier length requirements.

## 1. Introduction

Permanent abandonment of wells involves establishing cross-sectional barriers that shall prevent uncontrolled migration and release of formation fluids. Traditional abandonment designs have relied on cutting and pulling of tubing and casings or section milling of casings to access the annular and establish cross-sectional barriers. Currently, such operations require the capabilities of a drilling rig, which increases costs and the environmental footprint of the operation, and in the case of milling also the risk level of the operation. In cases where the original annular cement behind the production casing provides zonal

isolation, an alternative and cost-effective abandonment design is to isolate by setting a through-tubing cement plug, where tubing is left in the hole. As demonstrated by very recent field examples from a subsea abandonment campaign of four wells in the North Sea, the through-tubing abandonment plug can be set from a light-weight intervention vessel (Thom et al., 2020).

Successful annular fluid displacement is critical when isolating the well by setting through-tubing abandonment plugs. As described by Thom et al., the operation involves punching or cutting the production

\* Corresponding author at: University of Stavanger, P.O. Box 8600, 4036 Stavanger, Norway.  
E-mail address: [hans.j.skadsem@uis.no](mailto:hans.j.skadsem@uis.no) (H.J. Skadsem).

<https://doi.org/10.1016/j.petrol.2022.110717>

Received 11 March 2022; Received in revised form 11 May 2022; Accepted 29 May 2022

Available online 4 June 2022

0920-4105/© 2022 The Author(s). Published by Elsevier B.V. This is an open access article under the CC BY license (<http://creativecommons.org/licenses/by/4.0/>).

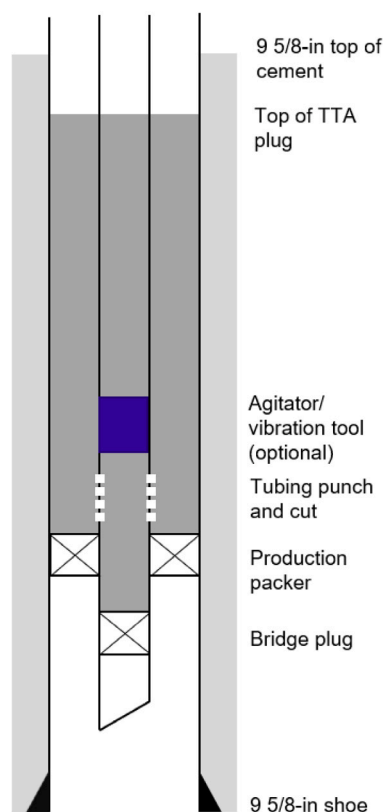


Fig. 1. Schematic of a well after placement of the through-tubing abandonment (TTA) plug. The potential impacts of the indicated vibration tool on the annular fluid displacement is the main topic of this study.

tubing above the production packer, and installing a bridge plug toward the bottom of the tubing, Thom et al. (2020). The cement slurry is next injected down the well inside the tubing and flows back toward surface in the A-annulus behind the tubing. The packer and bridge plug ensures that the cement slurry is directed into the A-annulus, as intended. At the end of the operation, cement slurry fills the interior of the tubing and the A-annulus. The operation leaves the production tubing behind in the well, and thereby circumvents the need for the pulling capacity of an offshore drilling rig (Thom et al., 2020). A schematic illustrating the through-tubing plug configuration is provided in Fig. 1. The flow-through vibration tool indicated in the figure will be discussed in more detail below.

In most cementing operations, whether for primary cementing of casings or liners or for setting of through-tubing abandonment plugs, the tubing or casing to be cemented is not perfectly concentric within the borehole. Tubing or casing eccentricity results in variable gap width around the annulus, which in turn produces a variable axial flow velocity. As the eccentricity increases, the velocity on the narrow side of the annulus decreases due to the close proximity of the tubing or casing and borehole walls. For yield stress fluids, such as most drilling fluids, extreme eccentricities can render the narrow side static, so that only fluid from the wider sector of the annulus is replaced while pumping (Walton and Bittleston, 1991; Szabo and Hassager, 1992). The resulting mud channel on the narrow side can result in compromised zonal isolation and fluid migration behind the tubing or casing (McLean et al., 1967; Wilson and Sabins, 1988). Undesirable effects of eccentricity is normally mitigated by installing centralizers along the casing string, to ensure a minimum stand-off at particularly the lower part of the casing during primary cementing (Guillot and Nelson, 2006; Torsvoll et al., 1991; Jung and Frigaard, 2022). On the other hand, production tubings in most mature wells that are now approaching the abandonment

phase were not designed with through-tubing abandonment in mind, and hence are not centralized. The placement of a through-tubing abandonment plug therefore needs to consider possibly highly eccentric annuli.

Fluid rheologies and displacement rates can help improve displacements in eccentric annuli. For primary cementing, the casing may sometimes also be rotated or reciprocated in an attempt to improve displacement along the narrow side of the annulus. Rotating the casing will promote azimuthal flow and direct displacing fluid from the wide to the narrow side of the annulus, and thereby partly compensate the effect of eccentricity on displacement (Al-Baiyat et al., 2019). Casing reciprocation is an option when the casing cannot be rotated, and will primarily serve to yield and mobilize fluid along the narrow side of the annulus. Previous work related to effects of casing movement on annular displacements encompass both computational and experimental studies. Examples of the former include the study by Carrasco-Teja and Frigaard who used a gap-averaged model for narrow annuli to identify conditions for traveling wave displacements in horizontal and near-horizontal wellbores (Carrasco-Teja and Frigaard, 2009, 2010). A similar numerical model was developed by Tardy and Bittleston, and used to show how inner casing rotation can partly compensate eccentricity and result in a less stretched fluid–fluid interface (Tardy and Bittleston, 2015). More recently, Enayatpour and van Oort conducted fully 3D numerical simulations of non-Newtonian fluid displacements and showed that casing rotation becomes more effective as inner casing eccentricity increases (Enayatpour and van Oort, 2017). Similar observations were also reported by Bu et al. who used a combination of 3D simulations and displacement experiments to study the effects of casing rotation in near-horizontal annuli (Bu et al., 2018). Their results show that the displacement efficiency generally improved with increasing casing rotation speed, up to a speed of 40 revolutions per minute (Bu et al., 2018). Reciprocation is generally simpler to implement in practice for cementing of casings, but it is considered less effective in improving fluid displacement compared to rotating the casing (McLean et al., 1967).

Placement of the through-tubing abandonment plug is faced with similar challenges as primary cementing of casings, involving a relatively narrow and eccentric annular space, and an *in-situ* fluid, normally a completion brine, that may have been static for a considerable period of time. Further, if the completion brine has been contaminated with formation fluids or clays, it may have developed high viscosity and even yield stress behavior. Finally, conventional casing rotation or reciprocation strategies do not apply for the production tubing. To still enable movement of the tubing for improving mobilization of completion brine and improving the annular displacement, agitator or vibration tools have become commercially available in recent years. In the recent field example discussed by Thom et al., such agitation tools were implemented with the goal of securing complete annular displacement (Thom et al., 2020). These agitator or vibration tools are similar to friction-reduction tools that are often used when sliding-drilling with a steerable mud motor; in the absence of drill string rotation, a considerable mechanical drag can accumulate along the drill string due to sliding friction. Generating axial and/or lateral vibrations can be effective in releasing some of the drag, and improve weight transfer to the bit, increase rate of penetration and reduce wellbore tortuosity (Gee et al., 2015).

When used as friction-reduction tools during drilling operations, these tools generate beneficial axial and/or lateral vibrations in the drill string as fluids are circulated through the tool. Axial vibration tools consist of a positive displacement motor and a valve section with an eccentric orifice, that generates pressure pulses as mud is pumped through. The pressure pulses propagate to a shock module of the tool, where a mandrel extends and retracts in response to the pressure pulse. The result is axial oscillations that propagate along the drill string in both directions from the oscillation tool (Gee et al., 2015), helping to reduce the drag and friction along the string. Lateral vibration tools

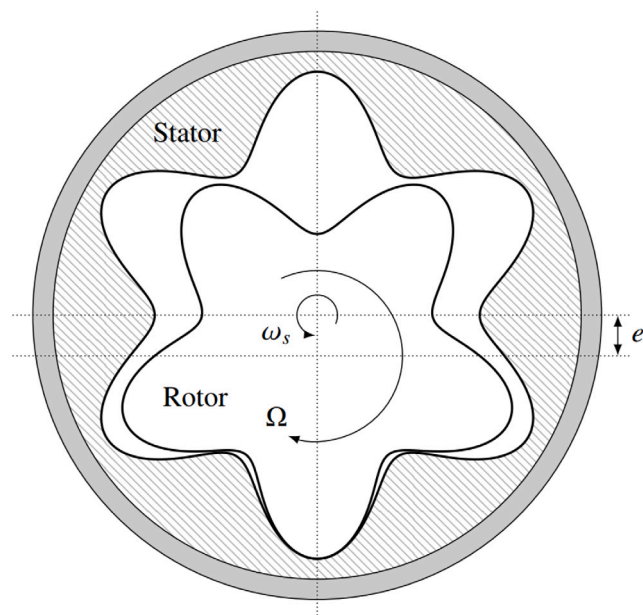


Fig. 2. Rotor and stator of a positive displacement motor with  $k = 5$  lobes and an eccentricity  $e$ . The relation between the motor speed  $\Omega$  and the angular velocity of the rotor is  $\omega_s = k\Omega$ . The figure is based on Ref. Heisig (1993).

normally set up vibrations through a turbine that drives an eccentric mass shown schematically in Fig. 2. The orbital movement of the rotor causes transverse vibrations that can reduce the normal force between string and bore hole wall, and also reduce drag due to mechanical friction. Gee et al. performed a computational study comparing the two means for generating vibrations, and reported field experience with such tools. Their analysis showed that axial vibrations propagate further than lateral vibrations that are excited by the same amplitude and frequency (Gee et al., 2015).

The purpose of this study is to study the potential benefits of agitation or vibration tools on annular fluid displacements, focusing primarily on the lateral movement of the tubing. Previous studies of lateral or orbital motion of the inner pipe have been mainly connected to friction pressure losses and cuttings transport in drilling operations. Vieira Neto et al. reported friction pressure measurements acquired by pumping a shear thinning fluid through an annular section where an eccentric inner pipe could be rotated about the center axis of the outer pipe (Vieira Neto et al., 2012). More recently, Bicalho et al. performed a combined experimental and numerical study of orbital drill string motion using a similar experimental configuration, but with a partially blocked eccentric annulus, Bicalho et al. (2016). Results from both studies show that fluid viscosity, volumetric flow rate and eccentricity significantly affect the annular pressure drop, and that the orbital motion of the inner pipe had a minor effect (Vieira Neto et al., 2012; Bicalho et al., 2016). Cayeux et al. considered the case of synchronous whirl as a mechanism for one-sided tool-joint wear, and calculated friction pressure gradients for Newtonian, power law and Herschel-Bulkley fluids in an eccentric annulus with a whirling drill string (Cayeux et al., 2018). For the relatively narrow annulus and the rotational speeds considered, it was found that the friction pressure gradient is not severely influenced by the orbital component, implying that synchronous whirl and a fixed, rotating drill string would give rise to approximately the same friction pressure drop (Cayeux et al., 2018). Effects of lateral drill string movement on the transport of cuttings in a horizontal wellbore have recently been investigated by Pang et al. (2019) and Busch and Johansen (2020) using computational methods. Both studies showed that orbital motion of the drill string leads to significantly improved cuttings transport compared to the case of a

fixed eccentric drill string that simply rotates about its own axis. The orbiting and whirling motion of the drill string was found to reduce the peak axial velocities between the wide and narrow sides of an eccentric annulus, and to agitate the cuttings bed on the low side of the borehole resulting in improved transport conditions (Pang et al., 2019; Busch and Johansen, 2020).

We report a combined experimental and computational investigation of the effectiveness of tubing vibration on annular displacements. Fluid displacement experiments have been performed to investigate the effects of transverse vibrations at vertical, inclined and near-horizontal inclinations using an annular test section capable of transverse, orbital motion of the inner tubing which replicates the lateral motion generated by a positive displacement motor, as shown in Fig. 2. We focus on the displacement of a yield stress fluid that, in the absence of tubing vibrations, remains static along the narrow side of the eccentric annulus. This first study of vibration-assisted displacements will assess how lateral movement of the inner tubing can yield the fluid and improve the annular displacement. A computational fluid dynamics study has been performed to further explore the displacement mechanism observed in the experiments, and finally a vibration analysis has been undertaken to explore the spatial decay of vibration amplitudes, and over what length of the well the potentially beneficial vibrations are active.

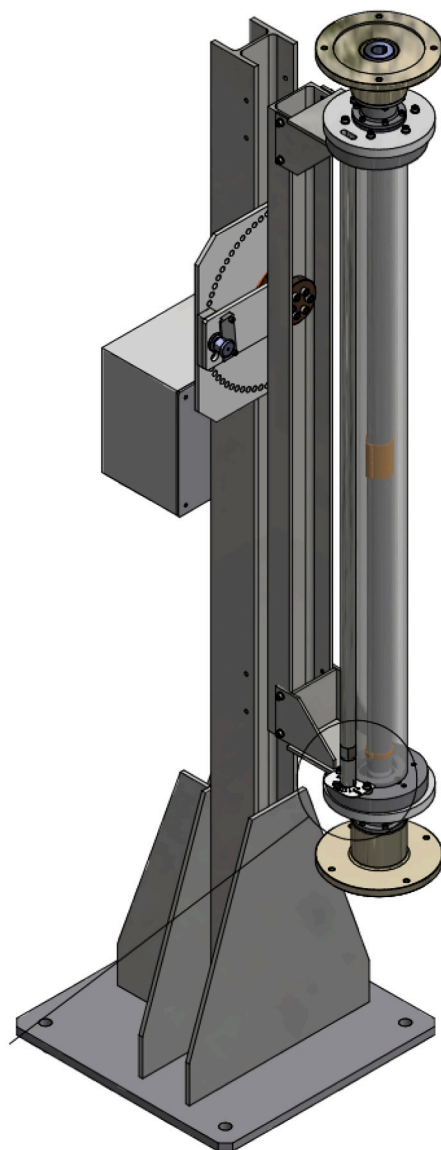
The outline of the paper is as follows. Our experimental and computational methodology is introduced in Section 2. Results of the experimental study are presented in Section 3. Further insights into how lateral vibrations affect mud displacements is provided by results of the computational fluid dynamics study, reported in Section 4. Finally, results of the mechanical vibration analysis are provided in Section 5. Finally, we conclude the study in Section 6.

## 2. Methodology

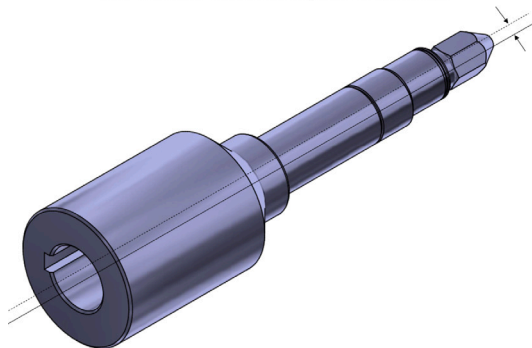
### 2.1. Experimental setup and test fluids

The experiments were conducted using a dedicated test rig that consists of an annular test section and a frame that allows the test section to be oriented at any inclination. A schematic of the test rig is provided in Fig. 3(a), where the annular test section is oriented vertically. The test section consists of an inner tubing that can be centralized or placed off-center by a distance  $\delta$  within the outer, transparent pipe. Fluids are injected through an inlet port installed at one side of the bottom end cap, and collected at an outlet port installed at the same side of the top end cap. The centralization of the inner tubing is adjustable to allow the study of displacements in a concentric annulus and at different levels of eccentricity. A special feature of the test rig is that the inner tubing is mounted onto an eccentric drive shaft shown in Fig. 3(b). A motor mounted at the top of the test section rotates the drive shaft, which in turn makes the inner tubing orbit about its center location. The inner tube is mounted onto the eccentric drive shaft with bearings and a locking pin ensures that the inner tube only makes a translational motion within the outer pipe, and does not rotate about its own axis as the drive shaft rotates. This design is considered to replicate the lateral or orbiting movement of the tubing that is generated by a positive displacement motor used in commercially available vibration tools. The design is also similar to that previously used by Vieira Neto et al. and Bicalho et al. to study the friction pressure loss of non-Newtonian fluids in an eccentric annulus with orbiting motion of the inner tubing (Vieira Neto et al., 2012; Bicalho et al., 2016).

A Verderflex Rollit 25 hose pump fitted with an inline pulsation dampener was used to pump fluids through the test section. A constant flow rate of 6 l/min was used in all experiments. The displaced fluid was prepared by mixing tap water and 0.3 weight percent xanthan gum to produce a non-Newtonian fluid that was found to exhibit yield stress and shear thinning behavior. The fluid viscosity was measured using an Anton Paar MCR 301 rheometer with the results provided in



(a) Schematic of annular displacement test rig.



(b) Eccentric drive shaft for generating orbital motion of inner tubing.

Fig. 3. Drawings of the eccentric annulus test rig and the eccentric drive shaft that enables orbital motion of the inner tubing.

Fig. 4. The solid line in the figure corresponds to a least-squares fit to the measurements using the Herschel–Bulkley model  $\tau = \tau_y + K\dot{\gamma}^n = (3.96 + 0.28\dot{\gamma}^{0.56})$  Pa, where  $\tau$  and  $\dot{\gamma}$  denote the shear stress and the shear rate, respectively, and  $\tau_y$ ,  $K$  and  $n$  are the yield stress, consistency

Table 1

Summary of experimental setup and fluid properties used in the displacement experiments.

Parameter	Value
Tubing diameter, $D_i$	50.5 mm
Outer pipe inner diameter, $D_o$	70 mm
Length of test section	1516 mm
Vibration frequency, $f$	0 Hz, 2.48 Hz, 4.95 Hz, 10 Hz
Drive shaft offset, $a$	1 mm
Displacement flow rate	6 l/min
Annulus eccentricity, $e'$	0, 0.7
Displaced fluid density, $\rho_2$	998 kg/m <sup>3</sup>
Displaced fluid viscosity, $\mu_2$	$(3.96 + 0.28\dot{\gamma}^{0.56})/\dot{\gamma}$ Pa s
Displacing fluid density, $\rho_1$	1110 kg/m <sup>3</sup>
Displacing fluid viscosity, $\mu_1$	0.0025 Pa s

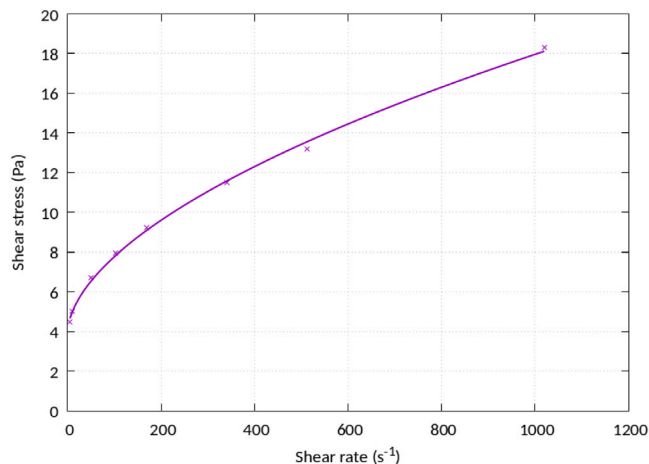
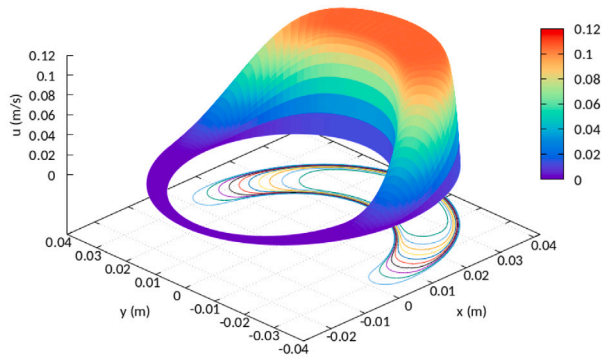


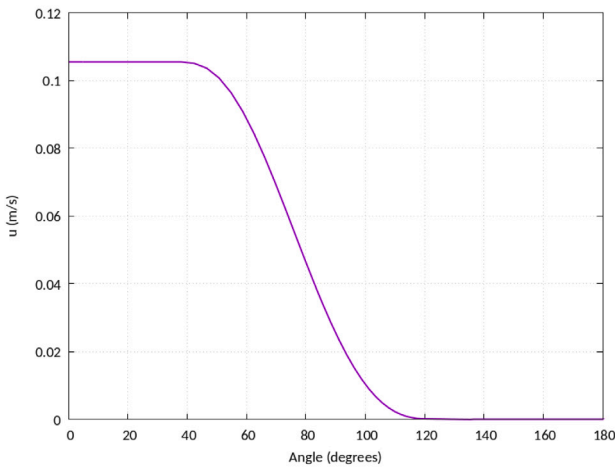
Fig. 4. Flow curve for displaced fluid and Herschel–Bulkley model parametrization,  $\tau_2 = (3.96 + 0.28\dot{\gamma}^{0.56})$  Pa.

index and the flow index, respectively (Herschel and Bulkley, 1926). The displacing fluid was prepared by mixing tap water with 20 weight percent sucrose and 0.0016 weight percent sodium chloride, and a water-soluble black ink to enable visual observation of the fluid–fluid interface during displacement experiments. In-line conductivity meters were installed at the inlet and at the outlet to the test section. The small addition of sodium chloride to the displacing fluid ensured different fluid conductivities, and allowed use of the conductivity meters for detecting arrival of the displacing fluid at the inlet and outlet. A summary of physical dimensions, experiment conditions and fluid properties are provided in Table 1. The radial ‘borehole’ clearance is  $(D_o - D_i)/2 \approx 9.75$  mm for the dimensions in Table 1, suggesting that the ratio of vibration amplitude to borehole clearance is approximately 0.1 in our experiments. For the parameters listed in Table 1, we estimate the concentric annulus entrance length to be approximately 0.10 m for the displacing fluid when using the two-dimensional channel result provided by Poole (2010). This development length is considered sufficiently short compared to the length of the test section. The more viscous displaced fluid is assumed to have an even shorter development length.

As mentioned in the introduction, the experiments were designed with the intention of maintaining stationary fluid along the narrow side of the eccentric annulus. Considering the displaced fluid viscosity model in Table 1 and a constant flow rate of 6 l/min, the fully developed, laminar velocity profile for the eccentric annulus is shown in Fig. 5. The velocity profile has here been obtained using the iterative solution algorithm described by Huilgol and You (2005). In Fig. 5(b), the velocity magnitude from the center of the annular gap is shown as function of azimuthal position. The angle is measured from the wide side of the annulus, where an unyielded region of constant velocity



(a) Velocity profile.



(b) Center line velocity.

Fig. 5. Fully developed velocity profile for the displaced fluid at a constant flow rate of 6 l/min in the  $e' = 0.7$  eccentric annulus.

is formed. Close to the narrow side, and starting at a position of approximately  $130^\circ$  from the widest side of the annulus, static fluid is predicted. In other words, during circulation or conditioning of the fluid to be displaced, a static layer is predicted along the narrow side, as intended for these experiments.

During displacement, the positive density hierarchy between the fluids aid in the displacement of the narrow side of the annulus. A criterion for predicting mobilization along the narrow side is provided by Théron et al. (2002),

$$\left(\frac{dp}{dL}\right)_1 + (\rho_1 - \rho_2)g \cos \theta > \frac{2\tau_{y,2}}{h}, \quad (1)$$

where  $(dp/dL)_1$  refers to the friction pressure gradient of the displacing fluid,  $\theta$  is the inclination from vertical, and  $h$  is the radial gap at the narrow side of the eccentric annulus. With  $\tau_{y,2} = 3.96$  Pa and  $h = 3$  mm, the combined friction pressure gradient and the pressure gradient due to the density difference should exceed about 2708 Pa/m in order to mobilize the narrow side. For the low-viscosity displacing fluid, we estimate  $(dp/dL)_1 \approx 10$  Pa/m, while the contribution due to the density difference itself is only about  $(\rho_1 - \rho_2)g \approx 1100$  Pa/m for a vertical annulus. Combined with Eq. (1), this suggests a static narrow side also during displacements, in the absence of vibrations.

Relevant dimensionless numbers that govern the displacement experiments include the geometric properties of the test section, such as the diameter ratio  $\kappa = 50.5/70 \approx 0.72$ , inner tubing eccentricity and test section inclination. Additional dimensionless numbers appear as ratios of different forces, such as the Reynolds number in each fluid,  $Re_i$ , and the densimetric Froude number,  $Fr$ . A summary of the dimensionless

Table 2

Dimensionless numbers for the displacement experiments.

Dimensionless number	Definition	Value
Aspect ratio, $\kappa$	$D_i/D_o$	0.72
Annulus eccentricity, $e'$	$2\delta/(D_o - D_i)$	0, 0.7
Inclination, $\theta$	From vertical	$0^\circ, 60^\circ, 80^\circ$
Atwood number, $At$	$(\rho_1 - \rho_2)/(\rho_1 + \rho_2)$	0.05
Reynolds number, $Re_1$	$\rho_1 U^* D_H/\mu_1$	469
Reynolds number, $Re_2$	$\rho_2 U^* D_H/\mu_2$	2.3
Froude number, $Fr$	$U^*/\sqrt{AtgD_H}$	0.54

numbers for the experiments described above is provided in Table 2. Here, the hydraulic diameter  $D_H$  is taken as characteristic length scale, and defined as the difference in pipe and tubing diameters. Further,  $\dot{\gamma}^* = 4U^*/D_H$  is taken as characteristic shear rate when estimating the displaced fluid effective viscosity, where  $U^*$  denotes the bulk axial velocity of the imposed flow. The imposed flow from the pump provided an axial bulk velocity of approximately 0.054 m/s. A characteristic angular velocity due to the orbital motion of the inner tubing may be estimated as  $2\pi f a$ , with  $f$  and  $a$  the vibration frequency and drive shaft offset from Table 1, respectively. We find the characteristic angular velocities of approximately 0.016 m/s, 0.031 m/s and 0.063 m/s at drive frequencies of 2.48 Hz, 4.95 Hz and 10 Hz, respectively. This result in ratios of orbital to axial bulk velocity of 0.29, 0.57 and 1.16, respectively.

As discussed above, the experiments involved the displacement of a non-Newtonian (yield stress, shear thinning) fluid by a denser Newtonian fluid. In the field, the annular space outside the production tubing is often assumed filled by a solids-free completion fluid, such as a brine. The completion fluid will be displaced by a cement slurry that normally would be denser and more viscous than the brine. The fluids used in the experiments are perceived to represent a conservative scenario, both in terms of the viscosity ratio and the relatively small density ratio (for comparison,  $At \approx 0.2$  for a cement slurry of density  $1920$  kg/m<sup>3</sup> displacing a  $1275$  kg/m<sup>3</sup> brine). As such, the experimental fluid configuration studied herein may represent a field case where the viscosity of the packer fluid has increased over time (e.g. due to contamination or degradation of the fluid), and where a lighter-weight cement slurry has been chosen in order to minimize the risk of stratification during placement in near-horizontal sections.

## 2.2. Computational methods

Details concerning the computational fluid displacement study and definition of a mechanical vibration model are provided below.

### 2.2.1. Computational fluid displacement simulations

Computational fluid displacement simulations were performed for the vertical, eccentric case defined in Table 1 using the open-source simulation software OpenFOAM, version 2112. Simulations were performed using the `interFoam` solver, which is specialized for two-phase, incompressible and immiscible fluids and where the volume-of-fluid method was used to track the position of the fluids in the annulus. For the vibration of the inner pipe, the Arbitrary Mesh Interface (AMI) functionality of OpenFOAM was used to dynamically morph the mesh during the simulation. A fixed harmonic oscillation was applied, where the motion of the inner pipe in the  $x$  and  $y$  direction was specified according to

$$x(t) = a \sin(2\pi f t) = a \sin(\omega_s t), \quad (2a)$$

$$y(t) = a \cos(2\pi f t) = a \cos(\omega_s t), \quad (2b)$$

with  $a = 1$  mm the amplitude and  $\omega_s = 2\pi f$  the angular frequency of the vibration.

The computational mesh consists of a structured mesh, which is graded towards the pipe walls and towards the narrow side of the

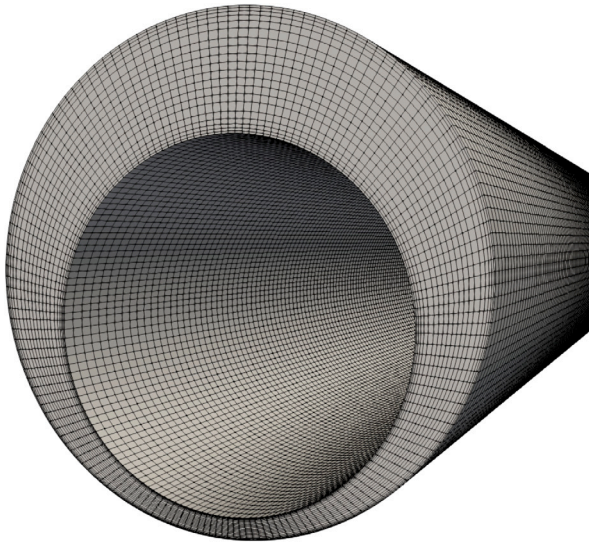


Fig. 6. Computational mesh used for the CFD simulations.

eccentric annulus. Based on an initial mesh sensitivity study, the mesh has 160 grid cells in the azimuthal direction, 20 cells in the radial direction and 500 cells in the axial direction, giving a total of 1.6 million cells. A picture of the mesh layout is shown in Fig. 6.

Second-order discretization schemes were used for the spatial terms and a first-order implicit scheme for the time discretization. To ensure a stable solution an adjustable time step was used with a maximum Courant number of 0.5. The Courant number in each cell is calculated as  $Co = 0.5\Delta t \sum U_f A_f / V$ , where  $f$  denotes the face of a cell,  $A$  is the face area and  $V$  is the cell volume. This gives a typical time step of  $\Delta t = 8 \times 10^{-4}$  s.

Numerical treatment of the non-Newtonian fluid is performed with a regularized Herschel–Bulkley rheology model where a threshold value for the viscosity is applied at very low strain rates:  $\mu_2 = \min \{ \mu_{2,0}, (\tau_{y,2} + K_2 \dot{\gamma}^{n_2}) / \dot{\gamma} \}$ . Here, this maximum viscosity is set to  $\mu_{2,0} = 1.7$  Pa s.

### 2.2.2. Tubing vibration analysis

The mechanical vibration analysis focuses on predicting the amplitude of induced vibrations at different positions above the location of the tool. To this end, a vibration model based on that of Christoforou and Yigit (1997) is used. For completeness, the model is introduced below. We focus on vibration amplitudes at relatively short distances above the tool, so borehole curvature is neglected for simplicity. That is, the borehole is assumed to have a constant inclination and azimuth over the length that is studied.

To facilitate the derivation of the model equations, the generalized Hamiltonian principle will be used (Goldstein et al., 2002; Rao, 2007):

$$\delta \int_{t_1}^{t_2} (U - T - W) dt = 0. \quad (3)$$

Here,  $U$  denotes the total strain energy in the tubing,  $T$  is the kinetic energy and  $W$  denotes the external work. We denote by  $u_1$  and  $u_2$  the transverse displacements, as shown in Fig. 7, and let  $u_3$  denote the axial displacement, which is taken positive in the direction of increasing measured borehole depth. Following Ref. Christoforou and Yigit (1997), the tubing is modeled as a uniform Euler–Bernoulli beam of length  $L$ , with the strain energy given by

$$U = \frac{1}{2} \int_0^L \left\{ EI (u_1''^2 + u_2''^2) + EA \left( u_3' + \frac{1}{2} (u_1'^2 + u_2'^2) \right)^2 \right\} dz, \quad (4)$$

where the notation  $u' = \partial u / \partial z$  has been introduced, and where finite strain introduces a coupling between axial and transverse displacements. Further,  $E$ ,  $I$  and  $A$  denote the Young's modulus of the

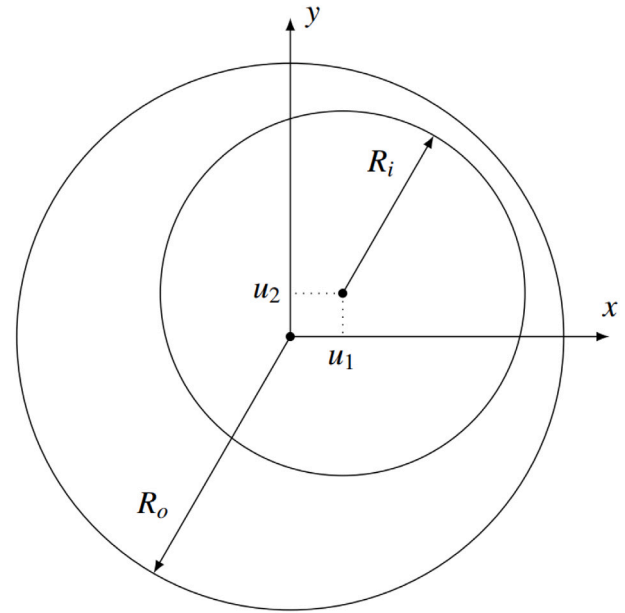


Fig. 7. Cross-section showing the transverse tubing displacement, measured relative to the center of the borehole.

tubing, the area moment of inertia and the steel cross sectional area, respectively. The tubing kinetic energy is taken as

$$T = \frac{1}{2} \int_0^L \rho A v^2 dz, \quad (5)$$

where  $v^2 = \dot{u}_1^2 + \dot{u}_2^2 + \dot{u}_3^2$ , and the notation  $\dot{u} = \partial u / \partial t$  has been introduced. The tubing steel mass density is denoted by  $\rho$ . The virtual work done by external forces such as gravity, viscous friction and borehole impacts is introduced similarly to Christoforou and Yigit (1997). Gravity is included by the virtual work  $\delta W_g$  as follows:

$$\delta W_g = \int_0^L \rho A g (\cos \theta \delta u_3 - \sin \theta \delta u_2) dz, \quad (6)$$

where  $\theta$  denotes the borehole inclination from vertical, and where we specify  $u_2$  to be positive in the direction of the high side of the borehole. Similar to Refs. Jansen (1991) and Christoforou and Yigit (1997), the viscous friction force is taken to be proportional to the square of the tubing velocity, i.e.

$$\delta W_h = -\rho_f C_D R_i \int_0^L |v| (\dot{u}_1 \delta u_1 + \dot{u}_2 \delta u_2 + \dot{u}_3 \delta u_3) dz, \quad (7)$$

where  $\rho_f$  and  $C_D$  denote fluid density and drag coefficient respectively, and where  $R_i$  is the outer radius of the tubing. Finally, the Hertzian borehole interaction model is used to capture impacts and sliding friction (Christoforou and Yigit, 1997):

$$\delta W_f = - \int_0^L K_H (r - b_{cl})^{3/2} \left\{ \left( \frac{u_1}{r} \delta u_1 + \frac{u_2}{r} \delta u_2 \right) + \mu \frac{\dot{u}_3}{|v|} \delta u_3 + \mu \text{sign} \left( \frac{\dot{u}_2}{u_1} \right) \left| \frac{v_i}{v} \right| \left( \frac{u_1}{r} \delta u_2 - \frac{u_2}{r} \delta u_1 \right) \right\} \delta(z - z_c) dz, \quad (8)$$

where  $K_H$  is the borehole stiffness parameter,  $b_{cl}$  is the radial clearance between the tubing and the borehole,  $\mu$  is the coefficient of sliding friction,  $r = \sqrt{u_1^2 + u_2^2}$  and  $|v_i| = \sqrt{\dot{u}_1^2 + \dot{u}_2^2}$  is the magnitude of the transverse tubing velocity. The Dirac delta function  $\delta(z - z_c)$  ensures that the impact and sliding friction forces are only active at positions  $z_c$ , where the tubing is in contact with the borehole wall, i.e. when  $r \geq b_{cl}$ . The first terms in Eq. (8) correspond to a normal impact force between borehole and the tubing. The consecutive terms which are proportional to  $\mu$  correspond to sliding friction. Since sliding friction always opposes

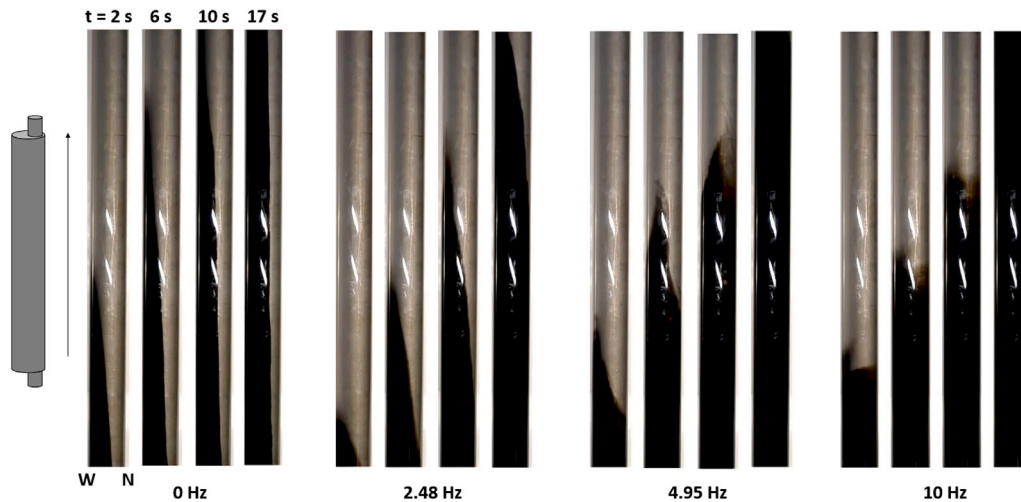


**Fig. 8.** Annular displacement in a vertical, eccentric annulus at different times (2 s, 6 s, 10 s and 17 s) after start of displacement, and different vibration frequencies. The labels 'W' and 'N' identify the wide (top) and narrow (bottom) sides of the annulus, respectively.

the net velocity direction, the axial and transverse velocity components are used to decompose the friction in these directions.

Finally, axial and transverse excitations are incorporated through boundary conditions at the bottom of the tubing. The axial excitation is assumed to be harmonic, with an angular velocity  $\Omega$ , equal to the motor output speed. The axial excitation amplitude is taken as the product of the pressure peak  $\Delta P$  generated by the oscillating valve inside the tool and the internal cross-sectional area,  $A_{in}$ . The lateral excitation is included in similar way as per Eq. (2), as harmonic forcing terms and following the approach of Heisig (Heisig, 1993): The vibration amplitude is taken as the centripetal force of the orbiting rotor shown in Fig. 2. Here the angular velocity of the rotor is given by  $\omega_s = k\Omega$ , with  $k$  the number of lobes in the rotor, Heisig (1993). To summarize, the following boundary conditions are applied at the bottom of the tubing:

$$EIu_1'''(z = L, t) = M_{rotor}e\omega_s^2 \cos(\omega_s t),$$

$$EIu_2'''(z = L, t) = M_{rotor}e\omega_s^2 \sin(\omega_s t),$$

$$EAu_3'(z = L, t) = \Delta PA_{in} \sin(\Omega t).$$

Generally, both  $\Delta P$  and  $\Omega$  will be determined by the pumping speed; a higher flow velocity is expected to increase the magnitude of both  $\Delta P$  and  $\Omega$ , and in effect also  $\omega_s$  and thereby the magnitude of the lateral excitations. In what follows, it is assumed that both  $\Delta P$  and  $\Omega$  are linearly proportional to the pumping speed. At the far end of the tool,  $z = 0$ , the tubing is assumed fixed and lying on the low side of the borehole. This is considered a reasonable approximation provided the computational domain (essentially the length  $L$ ) is sufficiently long so that the vibrations are not significantly affected by the fixed upper boundary condition. The governing equations defined above, and the associated boundary conditions, have been solved numerically using second order finite differences and a first order Euler method for time stepping.

### 3. Experimental results

As specified in Table 2, displacement experiments have been performed for vertical annulus and for inclinations corresponding to 60° and 80° measured from the vertical. In the following, main results will be presented per inclination, starting with the vertical configuration.

#### 3.1. Vertical annulus

In Fig. 8, photographs of the eccentric annular displacements are shown at 2 s, 6 s, 10 s and 17 s after start of displacement for the

static tubing (0 Hz). The labels 'W' and 'N' in the lower left corner indicates the orientation of the wide ('W') and narrow ('N') side in each photograph. Also shown are photographs from displacement experiments where the tubing is vibrated laterally at three different vibration frequencies.

The displacement in the vertical, eccentric and static tubing configuration in Fig. 8 resulted in channeling along the wide side for the injected, displacing fluid, and immobilized, residual fluid along the narrow side. Residual, static fluid along the narrow side was expected based on the fluid design considerations discussed in Section 2.1. Toward the end of the experiment, the interface between the fluids was close to vertical, and continued injection of displacing fluid did not improve displacement along the narrow side.

An obvious improvement in the annular displacement was achieved when the inner tubing was vibrated, as seen for the three vibration frequencies in Fig. 8. At the lowest frequency of 2.48 Hz, the ratio of orbital to axial velocity was approximately 0.29, which still resulted in an elongated interface that propagated faster along the wide sector of the annulus. It was however also evident that the narrow side became mobilized by the movement of the tubing, as the photographs indicate a steady, slow advancement of the fluid interface along the narrow side.

At the intermediate vibration frequency of 4.95 Hz, the tip or front of the fluid interface can now be seen shifted away from the widest part and toward the side of the eccentric annulus, likely caused by the orbital motion of the eccentric tubing. At the highest frequency, 10 Hz, the fluid interface was close to horizontal, suggesting that this highest orbital velocity can be effective in compensating for tubing eccentricity. While any vibration is seen to improve the displacement, the higher frequencies provide the greater displacement efficiency.

Results from experiments performed in a vertical and concentric annulus are not included. The symmetric, concentric annulus did not result in channeling effects. Consequently, effects of lateral vibration of the tubing were not significant in improving the displacement efficiency.

#### 3.2. Inclined annulus, 60°

Experimental results for the concentric and eccentric inclined annulus configurations are provided in Figs. 9 and 10, respectively. We note that the photographs have been rotated to vertical, to make the presentation more compact.

As the injected, displacing fluid was denser than the displaced fluid, the concentric annulus configuration showed a tendency for the dense fluid to propagate along the low side of the inclined annulus. This

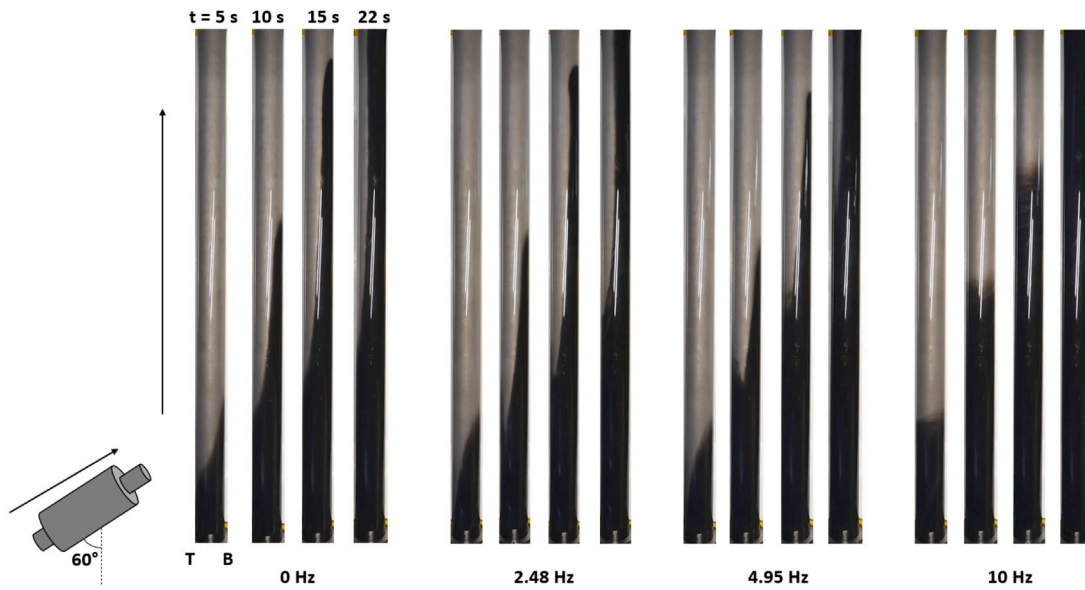


Fig. 9. Annular displacement in a 60° inclined, concentric annulus at different times (5 s, 10 s, 15 s and 22 s) after start of displacement, and different vibration frequencies. The labels ‘T’ and ‘B’ identify the top and bottom sides of the annulus, respectively.

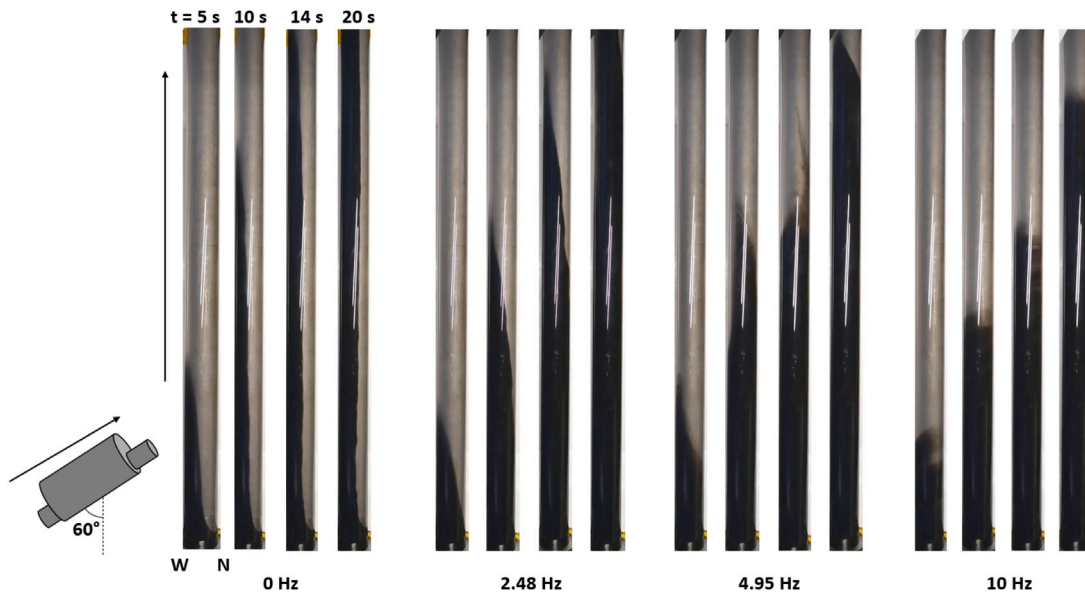


Fig. 10. Annular displacement in a 60° inclined, eccentric annulus at different times (5 s, 10 s, 14 s and 20 s) after start of displacement, and different vibration frequencies. The labels ‘W’ and ‘N’ identify the wide (top) and narrow (bottom) sides of the annulus, respectively.

tendency is observed both for static tubing and for the two lowest vibration frequencies, *i.e.* 2.48 Hz and 4.95 Hz. At 4.95 Hz vibration frequency, one can observe that the trailing edge of the fluid interface was not located at the top of the annulus, but appeared to be shifted to the side. This can be most clearly seen in the second photograph at 4.95 Hz in Fig. 9, and was most likely caused by the transverse velocity component developed by the vibrating tubing. As per the results for the vertical and eccentric annulus, the highest vibration frequency was the most effective in improving displacement efficiency. As seen in the right series of photographs in Fig. 9, the tendency for stratification was close to eliminated, resulting in improved displacement efficiency.

Shown in Fig. 10 are displacement results at the same inclination but now with an eccentric annulus, with the narrow side to the low side of the hole. In the absence of vibrations, the displacing fluid still channels along the top, wide side of the annulus, similar to the vertical and eccentric annulus shown in Fig. 8. The displaced fluid yield stress

was sufficient to block the narrow side and result in stratification with the dense, displacing fluid above the static yield stress fluid. The effects of vibration in the inclined and eccentric annulus were also relatively similar to the case for the vertical geometry; the lowest vibration frequency was sufficient to make the fluid interface propagate along the narrow side, and increasing the frequency resulted in a progressively more piston-like displacement and improved displacement efficiency.

### 3.3. Near-horizontal annulus, 80°

Shown in Fig. 11 are results from a near-horizontal inclination of 80° and the eccentric configuration. As above, the case with a static tubing resulted in channeling of displacing fluid along the top, wide side of the annulus, and a region of un-yielded fluid along the narrow sector. Vibrations were effective in mobilizing the narrow side, and also here the largest vibration frequency is seen to be more effective

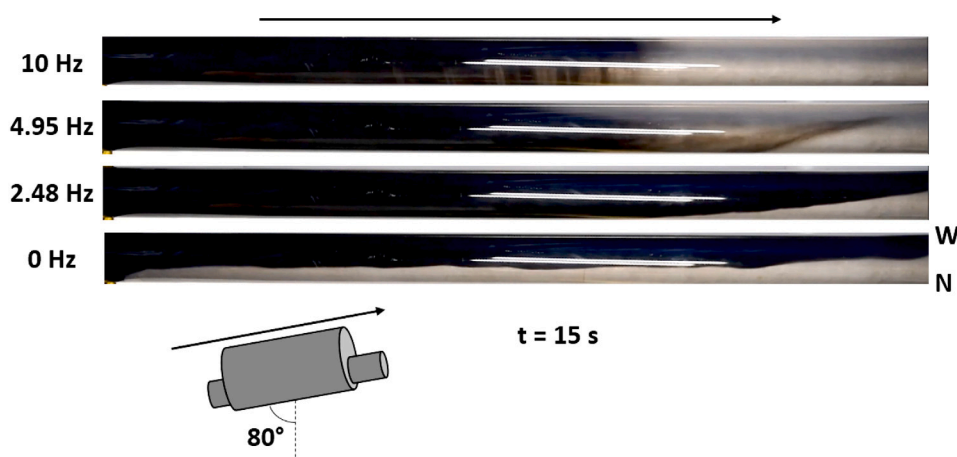


Fig. 11. Annular displacement in a 80° inclined, eccentric annulus at approximately 15 s after start of displacement for different vibration frequencies. The labels ‘W’ and ‘N’ identify the wide (top) and narrow (bottom) sides of the annulus, respectively.

in balancing the effect of eccentricity. Not shown are results from the near-horizontal and concentric annulus, as these experiments gave the same qualitative results as per the inclined, concentric annulus in Fig. 9.

To summarize, the experimental results discussed above indicate beneficial effects of vibration in both vertical and inclined configurations, and in both concentric and eccentric annuli. For the concentric cases considered, high vibration frequency was found to offset the tendency of the dense displacing fluid to stratify and occupy the low side of the annulus. For the eccentric cases, vibration yielded the displaced fluid along the narrow side, and counteracted the tendency toward wide side channeling of displacing fluid. In the vertical configuration, vibrations were found to result in a similar improvement as per the inclined annuli.

#### 4. Computational fluid dynamics analysis of vibration-assisted annular displacement

Numerical simulations of the displacement experiments have been performed for the highest vibration frequency of 10 Hz, and for the vertical and eccentric configuration. As the experiments discussed in Section 3 showed qualitatively similar trends at any annulus inclination, we choose to focus on the vertical configuration. Fig. 12 shows displacement results for the case of static inner tubing (left) and a vibrating inner tubing (right). In these panels, the wide side of the eccentric annulus is located to the left of the inner tubing.

As is evident from the left-most panels, corresponding to the case without vibrations, the interface propagates along the wide side only, leaving behind a significant portion of the narrow sector of the annulus. These results are in qualitative agreement with the experimental results in Fig. 8. The right-most panel in Fig. 12 clearly demonstrates the beneficial effects of lateral vibration of the inner tubing, resulting in a compressed, propagating fluid interface around the entire annulus. This result is also in excellent qualitative agreement with the experimental observations provided in Fig. 8.

To further examine the yielding of the displaced fluid, Fig. 13 shows a cross-section of the annulus containing only displaced fluid at time  $t = 6$  s. The figure shows the values of the instantaneous viscosity of the displaced fluid at an instant when the inner tubing is orbiting in the clock-wise direction, and now moving downward and to the left. The motion of the tubing displaces fluid out from the narrow side, and reduces the local viscosity by up to two orders of magnitude in these simulations. Interestingly, we observe what appears to be highly viscous pockets of fluid on either side of the narrow sector. These pockets are not attached to walls, and so will be transported axially with the imposed flow. We also observe that the fluid in the wide sector

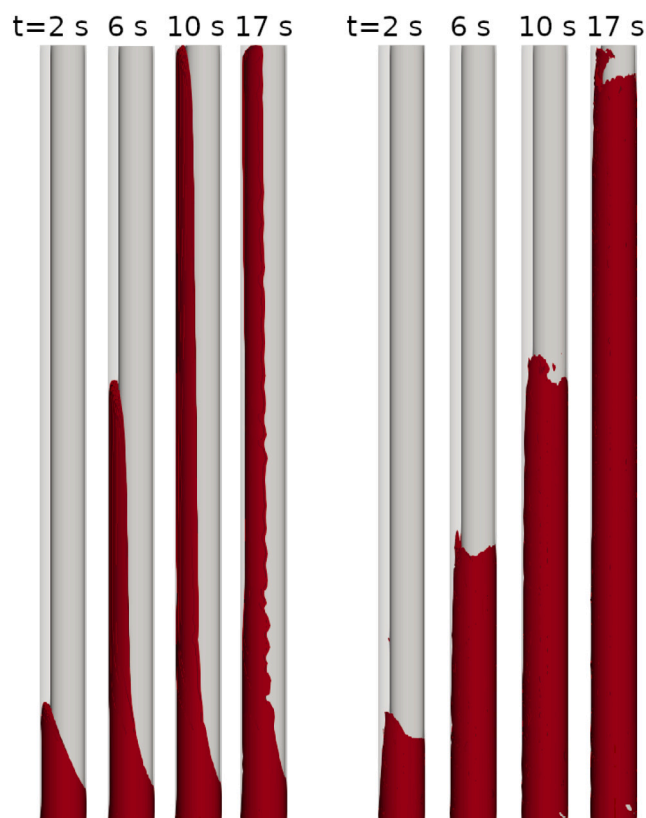


Fig. 12. CFD simulation of displacement in vertical, eccentric annulus with fixed inner pipe (left) and vibrating inner pipe (right). The oscillation frequency is 10 Hz.

of the annulus is yielded due to the azimuthal flow induced by the orbital motion of the inner tubing.

We explore the yielding and viscosity-reducing effect of the vibrating tubing in Fig. 14, where the viscosity of the displaced fluid is averaged over 10 periods of the vibration. Again, the comparison is made for only the displacing fluid, and static inner tubing (left) and 10 Hz vibrating tubing (right). The left panel in Fig. 14 presents the viscosity equivalent to the fully developed velocity profiles in Figs. 5(a) and 5(b). The viscosity at the narrow side attains the maximum value permitted by the numerical solver, and this region spans across the narrow gap, indicative of static and immobile fluid. Also in agreement with Fig. 5(a), an unyielded region exists in the center of the

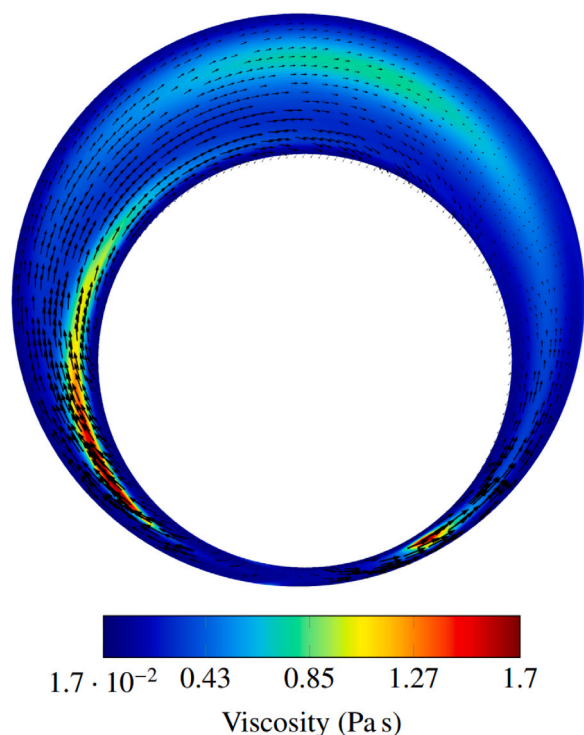


Fig. 13. Instantaneous viscosity and flow pattern in the displaced fluid at  $t = 6$  s.

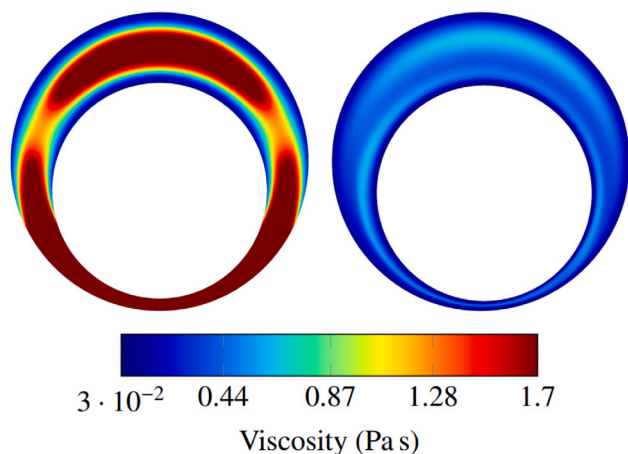


Fig. 14. Comparison of viscosity with fixed inner pipe (left) and oscillating inner pipe (right) at a constant imposed flow rate of 6 l/min. The oscillation frequency is 10 Hz and the viscosity is averaged over 10 periods.

wide sector, where the shear stress drops below the yield stress value of the displacing fluid. Connecting these two unyielded regions are *pseudo-plug regions*, where the axial velocity varies azimuthally, but not radially, [Walton and Bittleston \(1991\)](#). The beneficial effect of tubing vibration from a mud conditioning perspective is illustrated in the right panel, where now the vibration-averaged viscosity is clearly reduced over the full annulus cross-section compared to the case without vibrations.

Finally, in [Fig. 15](#) we compare the displacement efficiency for the numerical simulations of a vertical and eccentric annulus. The displacement efficiency is equivalent to the fraction of annular volume occupied by the *displacing* fluid ([Guillot and Nelson, 2006](#)), which is here plotted as a function of time since start of the displacement. In the initial phase of the simulations, where displacing fluid enters the domain from below and only the displaced fluid leaves the annulus at

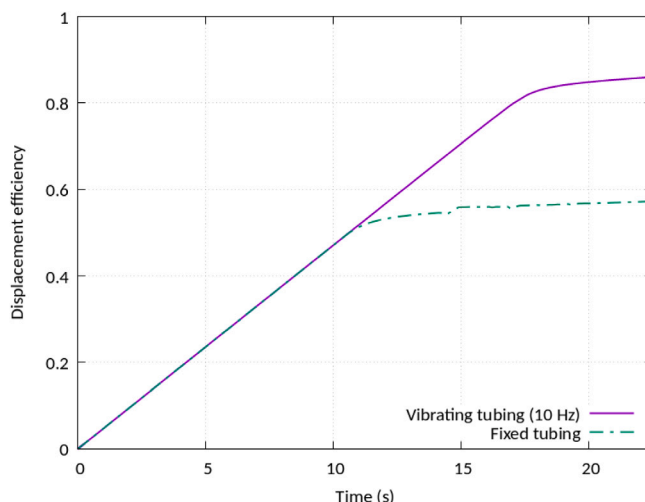


Fig. 15. Displacement efficiency for the displacement in a vertical, eccentric annulus with a fixed or vibrating inner tubing.

the top, the displacement efficiency increases linearly with a slope that corresponds to  $Q/V_0$ , or the ratio of the imposed flow rate to the total annular volume. The deviation from the initial linear trend corresponds to breakthrough of displacing fluid. As shown in [Fig. 15](#), and as seen in experiments and simulations, breakthrough happens sooner for the cases with a static inner tubing, as the displacing fluid now channels through the wide side and leaves most of the narrow side behind. Tubing vibration is seen to be effective in mobilizing the narrow side, which results in later breakthrough and a more complete displacement.

### 5. Vibration analysis

The experimental study and the supporting computational analysis presented above showed the effectiveness of lateral tubing vibrations in mobilizing and aiding the displacement of the original annular fluid. As seen from the dimensions of the experimental rig presented in [Table 1](#), the ratio of vibration amplitude to borehole clearance was only about 0.1 in the experiments and the computations. The results suggest that this relatively small amplitude can be efficient in aiding displacement, at least for the higher vibration frequencies considered.

A next step in the analysis of tubing vibrations is then to assess how far such vibrations can propagate along the tubing. This will be considered in the current section, using the mechanical vibration model defined in [Section 2.2.2](#) and typical dimensions for production tubings and production casings. For this part of the study, we assume the simulation parameters listed in [Table 3](#) with the tubing and borehole dimensions taken as per [Table 4](#). These cases are considered to represent typical tubing and casing dimensions relevant for cementing through-tubing abandonment plugs, and correspond to either a 177.8 mm (7-in.) and 46.7 daN/m (32 lb/ft) production tubing (case 1) or a 139.7 mm (5.5-in.) and 33.6 daN/m (23 lb/ft) tubing (case 2 and case 3). The borehole radius is given by the outer casing, which is taken as either a 244.5 mm (9 5/8-in.) and 78.1 daN/m (53.5 lb/ft) production casing (case 1 and 2), or a 177.8 mm (7-in.) and 33.6 daN/m (23 lb/ft) liner. Of these, case 2 results in the largest borehole clearance, followed by case 1 and with the 5.5-in. tubing in a 7-in. liner of case 3 producing the smallest annular clearance.

The motor frequency and axial and lateral excitation amplitudes listed in [Table 3](#) are based on commercial tool specifications. Further, a total axial length of  $L = 1000$  m is specified in [Table 3](#). This value corresponds to the length of the computational domain, where the harmonic excitation is applied at  $z = L$  and where the tubing at  $z = 0$  is

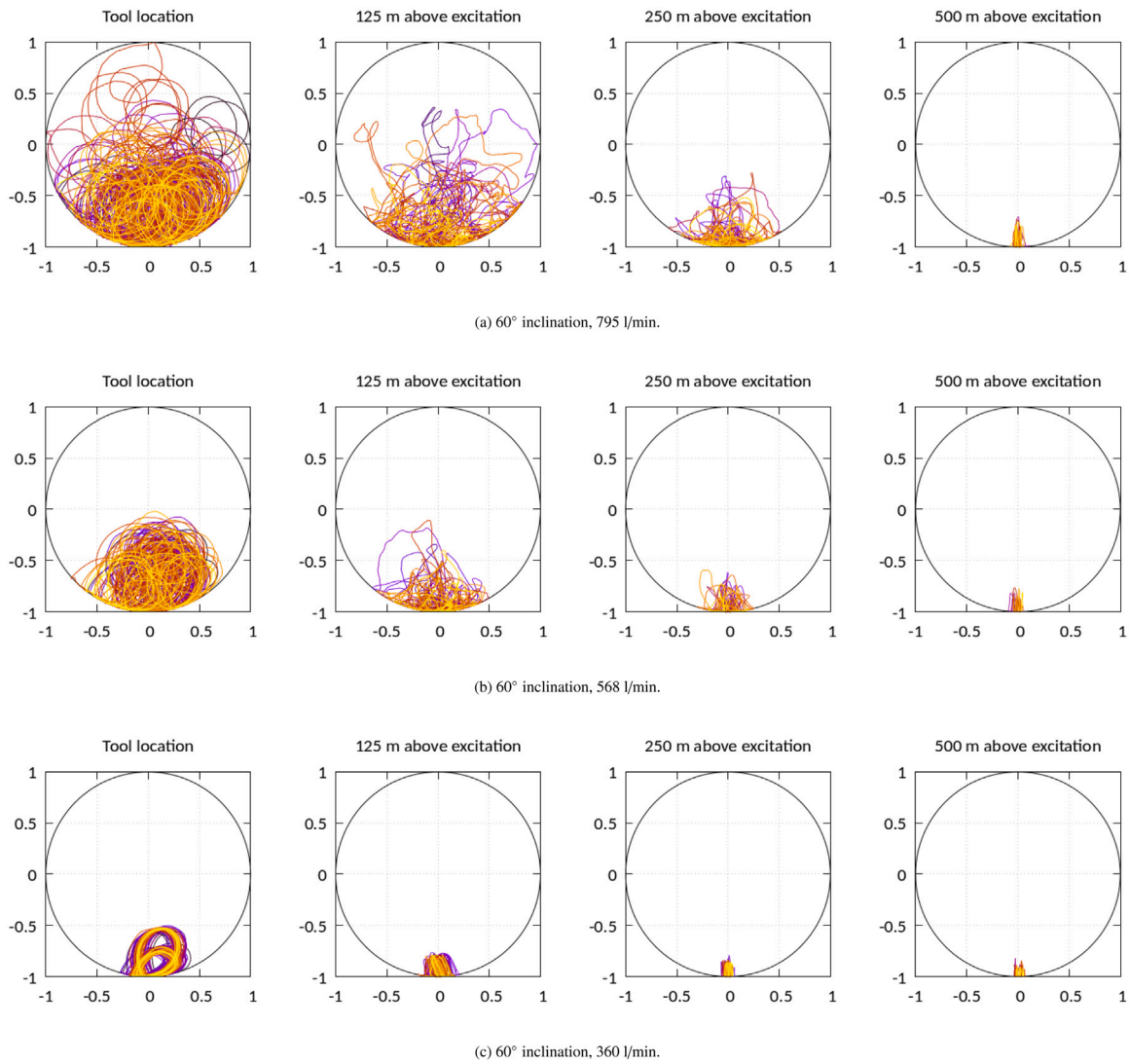


Fig. 16. Transverse displacements corresponding to the parameter values in Table 3 and case 1 in Table 4, at 60° inclination and different injection rates.

Table 3

Listing of fixed parameter values for the vibration analysis.

Quantity	Symbol	Value
Mass density steel	$\rho$	7850 kg/m <sup>3</sup>
Young's modulus steel	$E$	210 GPa
Simulation length	$L$	1000 m
Borehole stiffness	$K_H$	4.1–4.6 · 10 <sup>10</sup> N/m <sup>3/2</sup>
Borehole fluid density	$\rho_f$	1400 kg/m <sup>3</sup>
Fluid drag coefficient	$C_D$	1
Sliding friction coefficient	$\mu$	0.3
Inclination	$\theta$	60°
Motor frequency	$\Omega$	48.4 rad/s <sup>a</sup>
Number of lobes	$k$	5
Amplitude, axial exc.	$\Delta PA_{in}$	8.4 kN <sup>a</sup>
Amplitude, lateral exc.	$M_{rot}e\omega_s^2$	12.3 kN <sup>a</sup>

<sup>a</sup>The listed values are taken as representative for a pump rate of 795 l/min. The motor frequency  $\Omega$  and the pressure peak  $\Delta P$  are both assumed to be linearly proportional to the pump rate.

assumed to be fixed, as discussed in Section 2.2.2. Finally, the borehole stiffness coefficient,  $K_H$ , is determined by approximating the impact geometry as that of a spherical object impacting an elastic half-plane, suggesting that  $K_H \approx 2E\sqrt{R_o}/(3(1 - \nu^2))$ , where  $\nu$  is the Poisson ratio of steel (Johnson, 1985). Taking the outer radius of the two types of

Table 4

Listing of tubing and casing dimensions used in the vibration analysis.

	Quantity	Symbol	Value
Case 1	Tubing outer radius	$R_i$	0.0889 m
	Tubing inner radius	–	0.0774 m
	Borehole radius	$R_o$	0.1084 m
Case 2	Tubing outer radius	$R_i$	0.0699 m
	Tubing inner radius	–	0.0593 m
	Borehole radius	$R_o$	0.1084 m
Case 3	Tubing outer radius	$R_i$	0.0699 m
	Tubing inner radius	–	0.0593 m
	Borehole radius	$R_o$	0.0809 m

tubing listed in Table 4 suggests a stiffness coefficient in the range 4.1–4.6 · 10<sup>10</sup> N/m<sup>3/2</sup>.

Lateral displacements for case 1 in Table 4 (7-in. tubing in a 9 5/8-in. production casing) are shown in Fig. 16 for a constant inclination of 60° and three different driving frequencies (corresponding to three different injection rates). The lateral displacements have here been normalized by the borehole clearance,  $b_{cl}$ , which means that the normalized displacement amplitudes are confined to the interval [–1, 1]. The results suggest a significant sensitivity to the motor drive

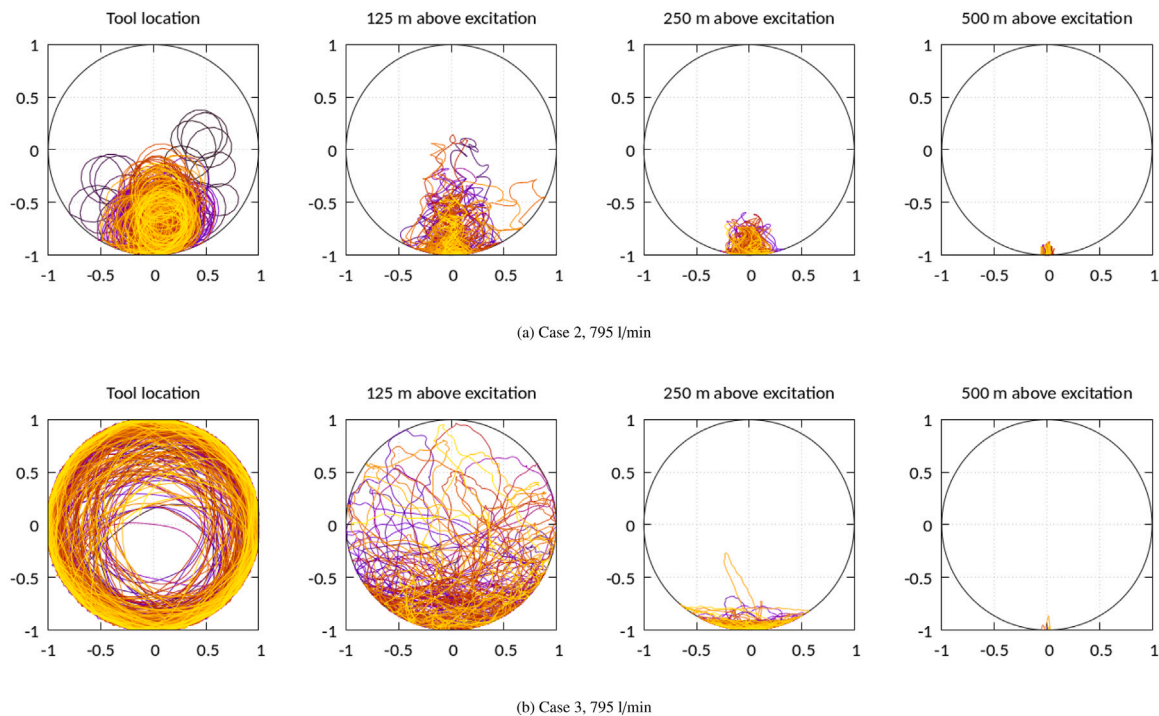


Fig. 17. Transverse displacements corresponding to the parameter values in Table 3 and cases 2 and 3 in Table 4, at different positions above the excitation source and for different borehole inclinations.

frequency, reflected through the different injection rates. This sensitivity is to be anticipated based on the transverse excitation amplitude being proportional to  $\omega_s^2 \sim \Omega^2$ . At the highest injection rate considered, corresponding to Fig. 16(a), the lateral displacement is significant at the position of the excitation, where the tubing orbits erratically around the borehole. Considerable lateral displacements are seen to propagate more than 250 m above the excitation source in this case, albeit with the tubing resting mainly on the low side of the borehole. We recall that the experiments and simulations reported above were performed with normalized lateral displacement amplitudes of approximately 0.1, so a similar effect may be expected as much as 250 m above the excitation point in this case.

Reducing the injection rate, and thereby the motor driving frequency, results in less agitation and more time spent sliding along the low side of the borehole, as seen in Figs. 16(b) and 16(c).

In Fig. 17, results are shown for cases 2 and 3 in Table 4, which correspond to a 5.5-in. production tubing inside a 9 5/8-in. casing or a 7-in. liner, respectively. The difference in borehole clearance is seen to have a significant impact on the lateral displacements. For case 2, which corresponds to the largest borehole clearance, the tubing is seen to mostly orbit about the lower side of the borehole at the level of the excitation. For case 3, which corresponds to the smallest borehole clearance of the cases considered, the radial gap is sufficiently narrow for the tubing to start whirling around the borehole circumference at the level of excitation. At 125 m above the excitation point, the tubing is seen to predominantly occupy the lower side of the borehole, although some erratic excursions toward the upper side still occur. At about 250 m above the excitation point, the tubing is predominantly oscillating along the lower side of the borehole, but still showing appreciable lateral motion compared to the conditions in the experiments and displacement simulations above.

To summarize, the vibration analysis presented above suggests that considerable vibration amplitudes are transmitted as much as 250 m above the vibration tool when operating at high displacement rates. This distance is greater than typical length requirements for permanent barriers, see e.g. Ref. NORSOK (2021). Since the amplitude of the lateral force developed by the vibration tool is assumed proportional to the

square of the displacement rate, the vibration amplitudes decrease correspondingly with decreasing displacement rates. Finally, we note that the above analysis is based on a straight borehole where the equilibrium position of the tubing is assumed to be on the low side of the borehole. This may be a reasonable first approximation for wells with small borehole curvature. In wells where curvature is more significant, locally large contact forces between tubing and casing can result in additional mechanical friction and more rapid decay of the lateral vibrations.

## 6. Summary and conclusions

Through-tubing abandonments of wells involve cementing the production tubing in place, an operation that can be performed using a light-weight intervention vessel (Thom et al., 2020). Placement of the through-tubing abandonment plug involves similar challenges as primary cementing of casings and liners, i.e. the need to mobilize and displace a resident fluid from a potentially highly eccentric and narrow annulus. This study has considered the effects of vibrating the tubing on displacing a yield stress fluid using a combined experimental and computational approach. Further, the characteristic propagation length of transverse vibrations have been studied using a combined axial-transverse vibration model.

The experiments consisted of density-stable and viscosity-unstable displacements, and showed the difficulty of displacing a static yield stress fluid from the narrow side of a highly eccentric annulus. The density ratio between the experiment test fluids was small, and insufficient to mobilize the narrow side. For displacement flows in the laminar regime, and in vertical or inclined annuli, increasing the density of the displacing fluid relative to the fluid to be displaced would likely lead to an improved displacement efficiency. In an operational context, this would represent the simplest solution for improving displacement along the narrow side. In cases where it is not possible or even desirable to increase the density ratio, such as at very high inclinations where a large density difference could result in significant stratification, this study shows that tubing vibrations can improve the displacement efficiency over the full range of inclinations. The larger vibration frequencies

results in the more significant improvements to the overall displacement. For the concentric and inclined annulus configurations, a high vibration frequency was found to be effective in opposing the tendency for stratification. The supporting computational study demonstrated that lateral tubing motion is effective in yielding and shearing the fluid in the annular gap, which significantly decreases the viscosity of the fluid and enabled complete displacement. Further, the vibration analysis demonstrated the dependency of propagation length on the displacement rate. For the cases considered, the highest displacement rate enabled tubing vibrations over lengths comparable to, and longer than common length requirements for permanent well barriers.

In conclusion, this combined experimental and computational study has shown that lateral tubing vibration can facilitate annular fluid displacements both in concentric and eccentric annuli during rig-less P&A operations where conventional reciprocation or rotation is not possible. This work is clearly limited in that only a single fluid pair and a fixed displacement rate has been used in experiments. Future work will investigate different fluid pairs, including fluids that are not necessarily static along the narrow side in the absence of vibrations, as well as increasing the density difference between the fluids to better represent the field situation of a light brine being displaced by a conventional slurry. The vibration model can be improved by introducing more sophisticated fluid–structure interaction and damping mechanisms, and to incorporate the effect of wellbore curvature. While the current study shows an example where vibrations clearly aid the displacement, future work should also attempt to identify conditions where such vibrations are potentially less effective aids.

#### CRedit authorship contribution statement

**Hans Joakim Skadsem:** Conceptualization, Methodology, Investigation, Writing – original draft, Writing – review & editing. **Knut Erik Teigen Giljarhus:** Investigation, Visualization, Writing – original draft. **Fiona Øijordsbakken Fredheim:** Methodology, Investigation. **Egbert van Riet:** Conceptualization, Resources, Supervision. **Wout J.G. Keultjes:** Resources, Supervision.

#### Declaration of competing interest

The authors declare that they have no known competing financial interests or personal relationships that could have appeared to influence the work reported in this paper.

#### Acknowledgments

The Petroleum Safety Authority Norway, AkerBP, ConocoPhillips, Petrobras, Shell and Total are acknowledged for financing the work through the P&A Innovation Program - a program for accelerating P&A technology development. The test rig used to perform displacement experiments with vibrating inner tubing was generously donated by Shell for the present and future studies. Ullrigg Test Centre is acknowledged for providing technical support that made the experiments possible.

#### References

Al-Baiyat, I., Khalil, M., Heinold, T., Porter, D., 2019. Production liner cementing practices in challenging horizontal wellbores. In: IPTC International Petroleum Technology Conference. IPTC-19471-MS, pp. 1–9. <http://dx.doi.org/10.2523/IPTC-19471-MS>.

Bicalho, I., dos Santos, D., Ataíde, C., Duarte, C., 2016. Fluid-dynamic behavior of flow in partially obstructed concentric and eccentric annuli with orbital motion. *J. Pet. Sci. Eng.* 137, 202–213. <http://dx.doi.org/10.1016/j.petrol.2015.11.029>.

Bu, Y., Tian, L., Li, Z., Zhang, R., Wang, C., Yang, X., 2018. Effect of casing rotation on displacement efficiency of cement slurry in highly deviated wells. *J. Nat. Gas Sci. Eng.* 52, 317–324. <http://dx.doi.org/10.1016/j.jngse.2018.01.040>.

Busch, A., Johansen, S.T., 2020. Cuttings transport: On the effect of drill pipe rotation and lateral motion on the cuttings bed. *J. Pet. Sci. Eng.* 191, 107136. <http://dx.doi.org/10.1016/j.petrol.2020.107136>.

Carrasco-Teja, M., Frigaard, I.A., 2009. Displacement flows in horizontal, narrow, eccentric annuli with a moving inner cylinder. *Phys. Fluids* 21 (7), 073102. <http://dx.doi.org/10.1063/1.3193712>.

Carrasco-Teja, M., Frigaard, I.A., 2010. Non-Newtonian fluid displacements in horizontal narrow eccentric annuli: effects of slow motion of the inner cylinder. *J. Fluid Mech.* 653, 137–173. <http://dx.doi.org/10.1017/S0022112010000212>.

Cayeux, E., Skadsem, H.J., Carlsen, L.A., Stokland, L.M., Cruikshank, S., 2018. Analysis of asymmetric tool-joint wear while drilling long horizontal sections. In: SPE Norway Subsurface Conference. SPE-191339-MS, pp. 1–24. <http://dx.doi.org/10.2118/191339-MS>.

Christoforou, A., Yigit, A., 1997. Dynamic modelling of rotating drillstrings with borehole interactions. *J. Sound Vib.* 206 (2), 243–260. <http://dx.doi.org/10.1006/jsvi.1997.1091>.

Enayatpour, S., van Oort, E., 2017. Advanced modeling of cement displacement complexities. In: SPE/IADC Drilling Conference and Exhibition. SPE-184702-MS, pp. 1–21. <http://dx.doi.org/10.2118/184702-MS>.

Gee, R., Hanley, C., Hussain, R., Canuel, L., Martinez, J., 2015. Axial oscillation tools vs. lateral vibration tools for friction reduction – What's the best way to shake the pipe? In: SPE/IADC Drilling Conference and Exhibition, Vol. Day 2 Wed, March 18, 2015. SPE-173024-MS, pp. 1–16. <http://dx.doi.org/10.2118/173024-MS>.

Goldstein, H., Poole, C., Safko, J., 2002. *Classical Mechanics*, third ed. Addison Wesley.

Guillot, D., Nelson, E.B. (Eds.), 2006. *Well Cementing*, second ed. Schlumberger, Sugar Land, Texas, US.

Heisig, G., 1993. *Zum Statischen und Dynamischen Verhalten von Tiefbohrsträngen in Räumlich Gekrümmten Bohrlöchern* (Ph.D. thesis). Technische Universität Braunschweig, Braunschweig, Germany.

Herschel, W.H., Bulkley, R., 1926. Konsistenzmessungen von Gummi-Benzollösungen. *Kolloid-Z.* 39, 291–300. <http://dx.doi.org/10.1007/BF01432034>.

Huilgol, R., You, Z., 2005. Application of the augmented Lagrangian method to steady pipe flows of Bingham, Casson and Herschel-Bulkley fluids. *J. Non-Newton. Fluid Mech.* 128 (2), 126–143. <http://dx.doi.org/10.1016/j.jnnfm.2005.04.004>.

Jansen, J., 1991. Non-linear rotor dynamics as applied to oilwell drillstring vibrations. *J. Sound Vib.* 147 (1), 115–135. [http://dx.doi.org/10.1016/0022-460X\(91\)90687-F](http://dx.doi.org/10.1016/0022-460X(91)90687-F).

Johnson, K.L., 1985. *Contact Mechanics*. Cambridge University Press.

Jung, H., Frigaard, I., 2022. Evaluation of common cementing practices affecting primary cementing quality. *J. Pet. Sci. Eng.* 208, 109622. <http://dx.doi.org/10.1016/j.petrol.2021.109622>.

Mclean, R., Manry, C., Whitaker, W., 1967. Displacement mechanics in primary cementing. *J. Pet. Technol.* 19 (02), 251–260. <http://dx.doi.org/10.2118/1488-PA>.

NORSOK D-010, 2021. *Well Integrity in Drilling and Well Operations*. Tech. rep., Standard Norge.

Pang, B., Wang, S., Jiang, X., Lu, H., 2019. Effect of orbital motion of drill pipe on the transport of non-Newtonian fluid-cuttings mixture in horizontal drilling annulus. *J. Pet. Sci. Eng.* 174, 201–215. <http://dx.doi.org/10.1016/j.petrol.2018.11.009>.

Poole, R.J., 2010. Development-length requirements for fully developed laminar flow in concentric annuli. *J. Fluids Eng.* 132, 064501, 1–4.

Rao, S.S., 2007. *Vibration of Continuous Systems*, first ed. John Wiley & Sons, Inc..

Szabo, P., Hassager, O., 1992. Flow of viscoplastic fluids in eccentric annular geometries. *J. Non-Newton. Fluid Mech.* 45 (2), 149–169. [http://dx.doi.org/10.1016/0377-0257\(92\)85001-D](http://dx.doi.org/10.1016/0377-0257(92)85001-D).

Tardy, P., Bittleston, S., 2015. A model for annular displacements of wellbore completion fluids involving casing movement. *J. Pet. Sci. Eng.* 126, 105–123. <http://dx.doi.org/10.1016/j.petrol.2014.12.018>.

Théron, B., Bodin, D., Fleming, J., 2002. Optimization of spacer rheology using neural network technology. In: SPE/IADC Drilling Conference and Exhibition. SPE-74498-MS, pp. 1–8. <http://dx.doi.org/10.2118/74498-MS>.

Thom, F., Angell, P., Greig, N., Robertson, N., Hogg, H., 2020. Case study for rig-less subsea well abandonment. In: SPE/ICoTA Well Intervention Conference and Exhibition, Vol. Day 2 Wed, March 25, 2020. SPE-199866-MS, pp. 1–16. <http://dx.doi.org/10.2118/199866-MS>.

Torsvoll, A., Olaussen, S., Almond, S., 1991. Keys to a successful cement job for a horizontal liner on statfjord a platform, well A-37A: A case history. In: SPE/IADC Drilling Conference and Exhibition, Vol. All Days. SPE-21970-MS, pp. 1–13. <http://dx.doi.org/10.2118/21970-MS>.

Vieira Neto, J.L., Martins, A.L., Ataíde, C.H., Barrozo, M.A.S., 2012. Non-Newtonian flows in annuli with variable eccentric motion of the inner tube. *Chem. Eng. Technol.* 35, 1981–1988. <http://dx.doi.org/10.1002/ceat.201200239>.

Walton, I.C., Bittleston, S.H., 1991. The axial flow of a bingham plastic in a narrow eccentric annulus. *J. Fluid Mech.* 222, 39–60. <http://dx.doi.org/10.1017/S002211209100099X>.

Wilson, M., Sabins, F., 1988. A laboratory investigation of cementing horizontal wells. *SPE Drill. Eng.* 3 (03), 275–280. <http://dx.doi.org/10.2118/16928-PA>.